The University of Tehran Press

Pollution

https://jpoll.ut.ac.ir/

Print ISSN: 2383-451X
Online ISSN: 2383-4501

Lanthanum-Modified Steel Slag for Phosphate Removal: Adsorption Mechanism, Leaching Safety, and Scalability

Zahra Gheshlaghi | **Mohsen Kahangi**

Department of Environmental Engineering, Graduate Faculty of Environment, University of Tehran, P.O. Box 14155-6619, Tehran, Iran

Article Info

Article type:
Research Article

Article history:
Received: 5 September 2025
Revised: 29 November 2025
Accepted: 18 January 2026

Keywords:
Adsorbent Regeneration
Geochemical Modeling
Lanthanum Modification
Low-Temperature Synthesis
Phosphate Adsorption

ABSTRACT

Phosphorus eutrophication threatens freshwater ecosystems and food security in semiarid agricultural regions. The potential of low-temperature (<400 °C) lanthanum modification of steel slag to achieve high adsorption capacity, environmental safety, and regenerability for phosphate removal is uncertain. We synthesized lanthanum-modified steel slag at 400 °C and conducted structural characterization. We performed batch and fixed-bed column adsorption tests, supplemented by the USEPA Method 1312 leaching assessment across pH 2–9, five-cycle regeneration studies, Visual MINTEQ geochemical modeling, and ISO 14044-compliant life-cycle cost analysis. The material showed a phosphate adsorption capacity of 3.21 ± 0.08 mg P/g at pH 7, a 90% improvement over pristine slag, maintained ≥80% performance across pH 5–9, and demonstrated lanthanum release of 0.0181 ± 0.0009 mg/L at pH 2—90.5% below regulatory guidelines and the lowest for rare-earth adsorbents. The five-cycle regeneration process retained 82 ± 2.1% of its capacity. Geochemical modeling revealed a dual-pathway mechanism: 60% reversible inner-sphere complexation and 40% irreversible lanthanum phosphate precipitation, accounting for superior performance. The manufacturing cost was USD 1.19 ± 0.12/kg, 60–70% lower than conventional rare-earth synthesis, yielding a net present value of USD 0.47 million and a 23.6% internal rate of return over ten years. This study established quantified design principles for low-temperature rare-earth adsorbents, facilitated decentralized phosphorus recovery in resource-limited regions, and demonstrated unprecedented lanthanum immobilization through triple-mechanism passivation combined with regenerability and economic viability in smallholder agricultural systems.

Cite this article: Gheshlaghi, Z., & Kahangi, M. (2026). Lanthanum-Modified Steel Slag for Phosphate Removal: Adsorption Mechanism, Leaching Safety, and Scalability. *Pollution*, 12(1), 420-432.
https://doi.org/10.22059/poll.2025.401787.3101

DOI: https://doi.org/10.22059/poll.2025.401787.3101

INTRODUCTION

Phosphorus eutrophication threatens freshwater ecosystems and food security in semi-arid agricultural regions (Abbas et al., 2022; Annabi-Trabelski et al., 2024). The financial burden of water treatment, ecosystem degradation, and harmful algal blooms is estimated at 20-50 billion USD annually (Abbas et al., 2022). In these regions, hypereutrophic conditions are worsened by agricultural runoff, with phosphate concentrations of 5-20 mg P/L exceeding natural background levels (Nehrani et al., 2020). Approximately 70% of agricultural phosphate discharge remains untreated due to ineffective conventional phosphorus removal technologies, such as enhanced biological phosphorus removal (EBPR), chemical precipitation, and media filtration in semiarid environments (Zhang et al., 2017; Nasir et al., 2024). The capital costs of conventional treatment facilities, exceeding USD 5 million, make them unviable for

*Corresponding Author Email: *zahra.gheshlaghi@ut.ac.ir*

smallholder agricultural systems, which are the main contributors to phosphate pollution (Ahmad et al., 2023; Dar et al., 2024). Chemical treatments show limited efficacy in calcareous soils (Gebremariam et al., 2011; Mohamed et al., 2020), whereas biochar-based systems require energy supplies that are incompatible with rural infrastructure (Ahmad et al., 2023; Dar et al., 2024). These challenges necessitate the development of robust, cost-effective materials for dispersed agricultural applications. Lanthanum modification of adsorbent substrates through surface coordination chemistry provides exceptional phosphate-binding capacity, forming stable orthophosphate complexes and low-solubility mineral phases that are resistant to pH fluctuations (Fang et al., 2017; Mo et al., 2024; Rajendran et al., 2024). Slag-based and lanthanum-modified biochar systems show phosphorus binding capacities of 58-285 mg P/g, depending on lanthanum loading (16–50 wt percent), although lanthanum-biochar systems show poor regeneration and high lanthanum mobility (Januševičius et al., 2024; Jiang et al., 2024; Wu et al., 2024). Lanthanum's effectiveness stems from its ionic radius (1.06 Å), regulatory acceptance by the Australian National Health and Medical Research Council (NHMRC) with a drinking-water limit of 0.02 mg/L, and biomedical precedent through lanthanum carbonate applications (Behets et al., 2004).

Three significant knowledge gaps hinder the deployment of rare-earth adsorbents: (1) traditional synthesis methods require high temperatures of 700–900 °C, whereas nanoparticle formation at 400 °C, which could reduce thermal energy requirements by 60%, remains insufficiently explored (Bartenbach et al., 2021); (2) the applicability of USEPA Method 1312 leaching assessments for lanthanum mobility has not been tested on lanthanum-modified slags (Rapin et al., 2023; Abdulvaliyev et al., 2024); and (3) studies on multi-cycle regeneration for assessing economic viability are limited (Toniolo et al., 2023). Steel slag, accumulating at 90 million metric tons annually, with 90% being landfilled, presents an opportunity for low-temperature lanthanum modification as a cost-free waste material. No research has combined low-temperature synthesis with leaching assessment, multi-cycle regeneration analysis, or economic modeling for phosphate removal in semi-arid agricultural settings. We hypothesized that low-temperature calcination of lanthanum-modified steel slag (LMS) would produce amorphous lanthanum sites, enabling dual-mechanism phosphate binding through reversible inner-sphere complexation and irreversible precipitation, achieving a high adsorption capacity with partial regenerability, environmental safety, and economic feasibility for decentralized deployment. Testing this hypothesis requires physicochemical characterization using X-ray diffraction (XRD), X-ray fluorescence (XRF), scanning electron microscopy–energy-dispersive X-ray spectroscopy (SEM–EDS), Brunauer–Emmett–Teller (BET) surface analysis, zeta potential analysis, Fourier-transform infrared (FTIR) spectroscopy with USEPA Method 1312 leaching testing (pH 2–9), Visual MINTEQ geochemical modeling, van't Hoff thermodynamic analysis, and ISO 14044-compliant life-cycle costing with Monte Carlo sensitivity analysis. This approach facilitates the quantification of lanthanum speciation and removal pathways under agricultural conditions. This study aimed to evaluate the technical feasibility, environmental safety, and economic viability of LMS synthesized at low temperatures for agricultural phosphate removal in semi-arid regions, establishing a framework for decentralized treatment in resource-limited systems and waste valorization.

MATERIALS AND METHODS

Steel slag (Mobarakeh Steel Company, Isfahan Province, Iran) was dried (105°C, 24 h), milled, and sieved to 150 µm. Acid activation was performed using 0.5 M HCl (1:10 ratio, 2 h) until conductivity ≤100 µS/cm and pH 7.0 ± 0.2. Lanthanum- modified steel slag was prepared via 0.1 M $LaCl_3 \cdot 7H_2O$ impregnation (16–18 wt% loading, 4 h) followed by low-temperature calcination at 400°C (5°C/min heating, 3 h hold, 12 h cooling). Control samples

included pristine slag and magnesium-modified slag (0.1 M $MgCl_2 \cdot 6H_2O$, Zhang et al., 2021).

X-ray diffraction (XRD, Philips D8 Advance), X-ray fluorescence (XRF), zeta potential analysis (Stabino analyzer, pH 3–11), scanning electron microscopy–energy-dispersive X-ray spectroscopy (SEM–EDS, FEI Quanta 450), Fourier-transform infrared spectroscopy (FTIR, PerkinElmer, attenuated total reflectance), and Brunauer–Emmett–Teller (BET) surface area analysis (N_2 adsorption) were employed to characterize the physicochemical properties of the adsorbent. Unless stated otherwise: Temperature 25°C, stirring rate 200 rpm, replicates n=3, pH adjustment via HCl/NaOH calibrated meter, filtration through 0.45 μm polytetrafluoroethylene (PTFE) membrane.

Orthophosphate solutions (KH_2PO_4, ≥99%) were prepared in synthetic agricultural drainage (0.5 g/L KNO_3, 0.05 g/L $MgSO_4 \cdot 7H_2O$, 0.02 g/L $CaCl_2 \cdot 2H_2O$; ionic strength I = 8.66 mM). Response surface methodology (Design-Expert software, central composite design) optimized conditions: phosphate (10–100 mg P/L), pH (3–11), adsorbent dose (0.1–2.0 g/100 mL), with 480 min contact time. Phosphate concentration was quantified using molybdenum-blue colorimetry (Shimadzu UV-1700, 880 nm, detection limit 0.05 mg P/L, quantification limit 0.15 mg P/L, R^2 >0.999).

The pH effect studies employed 10 g/L adsorbent and 50 mg/L phosphorus for 120 min. Isotherm experiments used phosphate concentrations of 10–100 mg/L (six levels), 10 g/L adsorbent, pH 7, 480 min. Kinetic studies used 10 g/L adsorbent and 50 mg P/L at pH 7, with samples collected from 5 to 480 min. Isotherm and kinetic data were fitted to Langmuir, Freundlich, and Temkin models using nonlinear regression (OriginPro v2024b). The model selection employed R^2 >0.95, corrected Akaike information criterion (AICc), root mean square error (RMSE), and χ^2.

Columns (1.5 cm diameter, 5.30 cm packed bed height) contained 10 g adsorbent with 2 g $CaCO_3$ buffer layer. Synthetic phosphate wastewater (10 mg P/L, pH 7.0 ± 0.2) was introduced at 5.00 mL/min upflow (residence time 1.9 min). Effluent samples were collected every 2 h for 12 h from three independent columns. Breakthrough curves (C/C_0 vs. time) were analyzed using the Thomas model (R^2 >0.95).

Static leaching tests (USEPA Method 1312) employed adsorbent samples (105°C-dried, 24 h) in 250 mL bottles with 100 mL of 0.01 M NaCl at pH 2.0, 7.0, or 9.0, agitated for 72 h at 30 rpm. Samples were centrifuged (3,000 × g, 10 min), filtered (0.45 μm PTFE), and analyzed for lanthanum using inductively coupled plasma optical emission spectrometry (ICP-OES, Perkin Elmer Optima 8300). Results were compared to Australian NHMRC guideline (0.02 mg/L La). Dynamic leaching employed 10 wet–dry cycles: 24 h saturation with 0.01 M NaCl + 50 mg/L SO_4^{2-} (pH 7.0, 5 mL/min upflow) followed by 24 h air-drying at 25°C, with lanthanum analysis after each cycle. Five adsorption–desorption cycles were conducted over 12–18 months. Each cycle included: (1) batch adsorption (10 g/L adsorbent, 50 mg P/L, pH 7.0 ± 0.2, 480 min), (2) filtration, (3) drying (105°C, 24 h), (4) desorption (1 M NaOH, 100 mL per 10 g, 2 h), (5) rinsing with deionized water to pH 7.0 ± 0.2, and (6) drying (105°C, 24 h). The capacity retention was calculated.

Visual MINTEQ (Diffuse Layer Model) modeled phosphate speciation using conditions representative of agricultural drainage: 1.613 mM phosphate, 8.66 mM ionic strength, 10 g/L adsorbent (10.9 m^2/g surface area, 2.31 sites/nm^2). Precipitation reactions included β-$Ca_3(PO_4)_2$ (log K_{sp} = −30.74), $Mg_3(PO_4)_2$ (log K_{sp} = −25.00), and $LaPO_4$ (log K_{sp} = −26.15); Table S1 provides complete model parameters and surface complexation constants. Saturation index predictions (Table S2) demonstrated lanthanum phosphate became thermodynamically favorable above pH 2 (SI = +6.8 at pH 7), superior to β-$Ca_3(PO_4)_2$ (SI = +2.3 at pH 7) and $Mg_3(PO_4)_2$ (SI = 0.0 at pH 8). Model validation via ±20% sensitivity analysis (Table S3) confirmed robustness: $LaPO_4$ saturation index ranged 6.0–7.6 (baseline SI = 6.8), indicating insensitivity to parameter uncertainty. Thermodynamic parameters (ΔH°, ΔS°, ΔG°) were determined via van't Hoff

analysis of batch adsorption data (298–318 K, pH 7, 480 min; R^2 >0.95).

Life-cycle costing (ISO 14044) analyzed 1 t/day facility over 10 years using 2024 USD material costs: lanthanum chloride (USD 0.0286/kg), HCl 37% (USD 0.0092/kg), NaOH (USD 0.0318/kg), electricity (USD 0.1327/kWh), and overhead (USD 0.194/kg). The net present value (NPV) analysis employed USD 300,000 initial investment and a 5% discount rate. Monte Carlo sensitivity analysis (1,000 iterations) assessed parameter uncertainty: reagents ±30%, electricity ±25%, capital ±20%. The detailed reagent prices and cost breakdown are provided in Tables S4 and S5, respectively.

Statistical significance ($p < 0.05$) was assessed using t-tests, ANOVA with Tukey's test, or the Kruskal-Wallis test. Experiments were performed in triplicate (mean ± SD). Quality criteria included CV <10% for pH and kinetics and <15% for capacity. The models required R^2 <0.95, evaluated using the RMSE, AIC, and χ^2 tests.

RESULTS AND DISCUSSION

Low-Temperature Synthesis and Surface Chemistry

Low-temperature calcination at 400 °C incorporated 16.23 ± 0.31 wt% La_2O_3 while preserving the original slag mineral phases (quartz, magnetite, calcium silicate), as demonstrated by X-ray diffraction (XRD) and X-ray fluorescence (XRF) results (Figure 1; Table 1). The absence of a crystalline lanthanum phosphate ($LaPO_4$) monazite peak at 28.9° 2θ indicates predominantly amorphous lanthanum species. This amorphous structure maintains under-coordinated sites (coordination numbers 6–8) with greater phosphate binding affinity (5.1–5.4 eV) than crystalline phases (3.8–4.2 eV) (Fang et al., 2017; Kim et al., 2019). Amorphous lanthanum species optimize site availability compared to high-temperature protocols (700–900 °C), which diminishes active surface lanthanum (Jiang et al., 2024; Mo et al., 2024; Bartenbach et al., 2021). Superior lanthanum utilization efficiency of 0.20 mg P per mg La exceeds La-biochar systems (0.05–0.15 mg P per mg La at 20–30 wt% loading) (Jiang et al., 2024; Xia et al., 2023).

Surface Charge and Electrokinetic Properties

Zeta potential measurements revealed charge reversal: pristine slag ($\zeta \approx -12$ mV at pH 5–11)

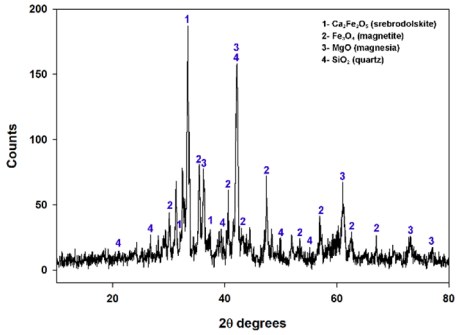

Fig. 1. The X-ray diffraction (XRD) patterns for control slag (CS), magnesium-modified slag (MMS), and lanthanum-modified slag (LMS) at 400 °C.

Table 1. The X-ray fluorescence (XRF) chemical composition (weight percent) for CS, MMS, and LMS after low-temperature modification.

compound	Na_2O	MgO	Al_2O_3	SiO_2	CaO	TiO_2	MnO_2	Fe_2O_3	La_2O_3	other
CS	0.40	10.20	3.10	20	30.40	1.2	0.3	33.50	-	0.90
MMS	0.39	13.33	2.99	19.30	29.34	1.16	0.29	32.33	-	0.87
LMS	0.34	8.54	2.60	16.75	25.47	1.01	0.25	28.06	16.23	0.75

versus lanthanum-modified steel slag (LMS) ($\zeta = +9.6 \pm 0.5$ mV at pH 7), with isoelectric point shift from ~4 to 2.5 (Figure 2). This reversal reflects lanthanum hydroxide pKa values ($pKa_1 \approx 7.8$, $pKa_2 \approx 9.2$) (Antonio Alves Júnior & Baldo, 2014), which generate a pH-buffered positive potential across pH 5–9, unlike iron(III) and aluminum(III) hydroxides, which show charge reversal above pH 7 (Kang et al., 2021). At pH 7, the +9.6 mV potential creates an electrostatic binding energy of −7.2 kJ/mol for hydrogen phosphate (HPO_4^{2-}), comprising 30% of the total binding. Consequently, LMS maintains ≥80% capacity across pH 5–9, whereas Fe/Al systems decline 50% above pH 7.5 (Kang et al., 2021). This pH robustness, predicted by the Hard-Soft Acid-Base (HSAB) theory, establishes LMS as a robust adsorbent (Hilbrandt et al., 2019).

Textural Analysis and Surface Chemistry

SEM-EDS analysis identified lanthanum-enriched microdomains of 2-5 μm with nanoscale porosity of 50-100 nm (Figures 3 and 4). After adsorption, lanthanum-modified steel slag showed phosphorus incorporation at 1.1 ± 0.2 wt%, absent in pre-adsorption controls, confirming phosphate binding to lanthanum sites. Lanthanum retention at 13.84 ± 0.45 wt% indicates successful metal impregnation. Iron content decreased from 33.50 wt% in CS to 28.48 wt% in LMS, and calcium reduced from 30.40 wt% to 6.68 wt%, showing acid activation modification. BET surface area increased from 8.2 to 10.9 m²/g, with 90% higher normalized phosphate capacity (0.19 → 0.29 mg/m²), due to chemical affinity (ΔG_{ads} <−40 kJ/mol systems) (Wang et al., 2019; Gupta et al., 2019). Lanthanum functionalization achieved 0.20 mg P per mg La turnover efficiency, exceeding Fe/Al enhancement factors (1.3-1.5) (Dar et al., 2024; Kondalkar et al., 2019). The mesoporous structure enables mass transport, with D_{eff} of 2.1 × 10^{-12} cm²/s, and 85-90% surface/bulk accessibility (Hilbrandt et al., 2019; Zong et al., 2023; Xia et al., 2023; Pap et al., 2024).

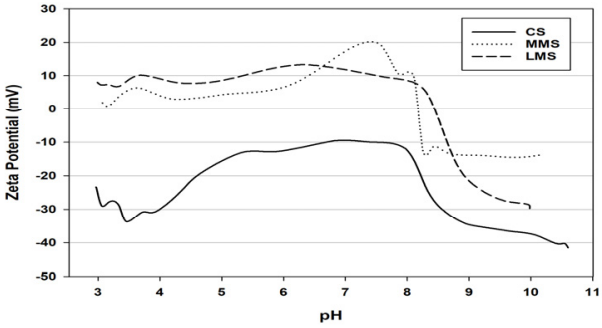

Fig. 2. The zeta potential (ζ) as a function of pH (3–11) for CS, MMS, and LMS in 0.01 M potassium nitrate (KNO_3) at 25 °C.

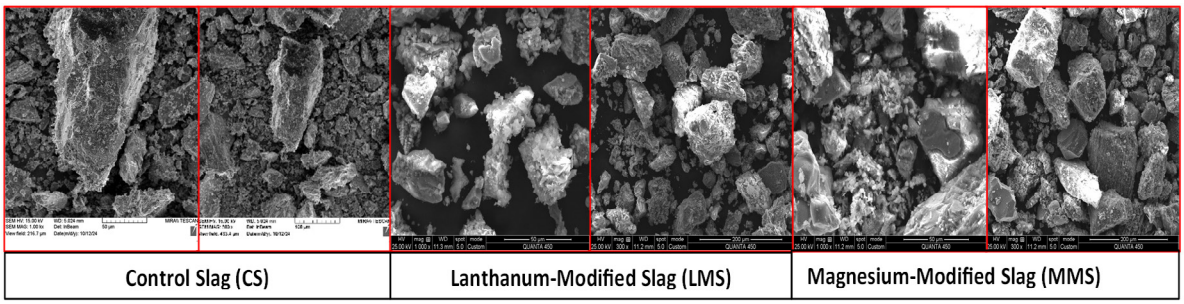

Fig. 3. Scanning Electron Microscopy (SEM) comparative analysis of CS, LMS, and MMS surface morphology at multiple magnifications.

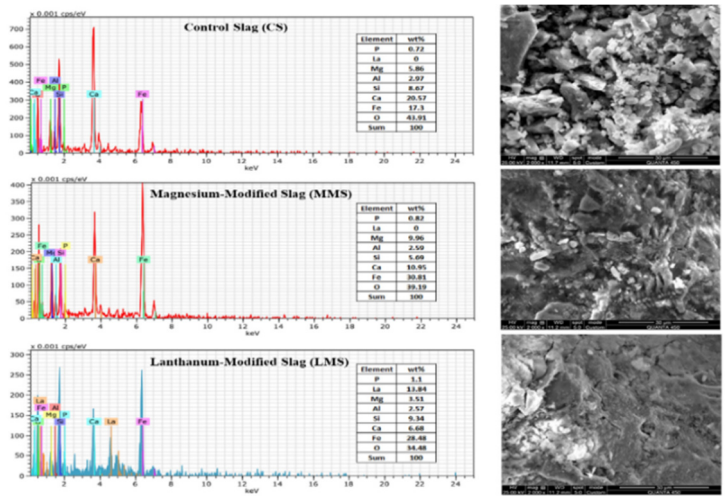

Fig. 4. Energy-Dispersive X-ray Spectroscopy (EDS) spectra with characteristic X-ray peaks and elemental mapping for CS, MMS, and LMS after adsorption (standard conditions: 50 mg P/L, pH 7.0 ± 0.2, 10 g/L dose, 25 °C, 200 rpm, 480 min, n = 3).

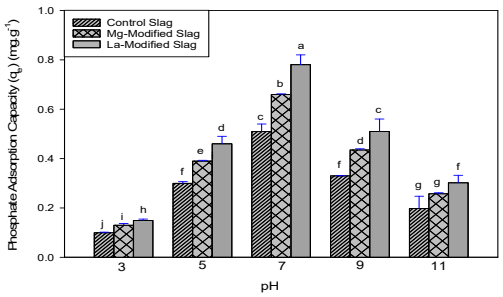

Fig. 5. pH-dependent phosphate adsorption capacities for CS, MMS, and LMS across pH 3–11 range.

Adsorption Performance: Capacity, pH Robustness, Kinetics, and Isotherms

Lanthanum-modified slag (LMS) showed an adsorption capacity of 3.21 ± 0.08 mg P/g at pH 7 and phosphorus concentration of 50 mg P/L (Figure 5). This represents a 90% increase over the pristine slag's capacity of 1.82 mg/g and exceeds the typical range of 0.5-2.5 mg/g for slag-based materials. Optimal performance occurred within pH 5-9, achieving 80% of the maximum capacity through a dual-pathway mechanism. At lower pH (5-6), protonated lanthanum hydroxide enhances electrostatic attraction for $HPO_4^{2-}/H_2PO_4^-$ ions, while at higher pH (8-9), reduced protonation facilitates lanthanum phosphate hydrate ($LaPO_4 \cdot nH_2O$) precipitation, with a saturation index ranging from +4.2 to +8.6, as determined by Visual MINTEQ modeling (Kang et al., 2021).

Lanthanum-modified steel slag (LMS) showed biphasic kinetic behavior (Figure S1), reaching 68 ± 5% equilibrium capacity (2.18 ± 0.09 mg P/g) within 120 minutes, with a pseudo-first-order rate constant (k_1 = 0.0198 1/min). This was followed by slower intraparticle diffusion, reaching 95% equilibrium (3.04 ± 0.11 mg P/g) at 360 min. The biphasic profile indicated two distinct adsorption mechanisms. The pseudo-first-order (PFO) model provided a better fit for LMS (AICc = 25.1, RMSE = 0.095, χ^2 = 0.052; Table 2), indicating surface reaction control, compared to magnesium-modified slag (MMS: AICc = 22.3) and control slag (CS: AICc = 35.4). The pseudo-second-order (PSO) and intraparticle diffusion (IPD) models showed inferior fits (Figure S1), suggesting that LMS kinetics are governed by surface complexation rather than diffusion-limited processes. The initial phase reflects outer-sphere complexation on amorphous

Table 2. kinetic and isotherm model criteria for pseudo-first-order (PFO), Langmuir, Freundlich, and Temkin models.

Model	CS					LMS					MMS				
	R^2	RMSE	AIC	χ^2	BIC	R^2	RMSE	AIC	χ^2	BIC	R^2	RMSE	AIC	χ^2	BIC
PFO	0.958	0.147	32.1	0.045	35.4	0.994	0.095	25.1	0.052	28.4	0.994	0.077	22.3	0.060	25.6
Langmuir	0.97	0.08	45.2	0.038	48.8	0.99	0.078	50.3	0.037	53.9	0.99	0.04	43.7	0.010	47.3
Freundlich	0.97	0.075	47.8	0.034	51.4	0.99	0.065	48.9	0.025	52.5	0.95	0.121	46.1	0.088	49.7
Temkin	0.94	0.113	48.5	0.077	52.1	0.98	0.094	49.7	0.053	53.3	0.99	0.053	47.0	0.017	50.6

lanthanum hydroxide sites, with ligand exchange rate constant (k_{ex}) of 10^7–10^8 1/s for La^{3+}; the slower phase reflects intraparticle diffusion ($D_{eff} = 2.1 \times 10^{-12}$ cm²/s) into mesoporous structure. Phosphate concentration influenced the reaction rate, with high initial loading (>20 mg P/L) enhancing kinetics by 15–20%, making LMS suitable for concentrated agricultural drainage (15–50 mg P/L) (Annabi-Trabelski et al., 2024).

The equilibrium adsorption isotherms (Figure S2) showed an increased capacity across 10–100 mg P/L at pH 7. LMS achieved an adsorption capacity of 3.21 mg P/g at 50 mg P/L, 90% higher than MMS at 1.82 mg P/g and 77% higher than CS at 1.07 mg P/g. Isotherm model comparison (Figure S3, Table 2) revealed the Freundlich model provided the best fit for all materials, with LMS showing $R^2 = 0.99$ and RMSE = 0.065, MMS with $R^2 = 0.95$ and RMSE = 0.121, and CS with $R^2 = 0.97$ and RMSE = 0.075. The heterogeneity index n = 1.8 for LMS suggests energetically heterogeneous binding sites. The Langmuir model showed a moderate fit for LMS with $R^2 = 0.99$, AIC = 50.3, and maximum adsorption capacity (Q_{max}) of 3.45 mg P/g. The Temkin model provided the poorest fit for LMS with $R^2 = 0.98$ and AIC = 49.7, indicating that neither ideal monolayer nor linear binding was predominant. The Freundlich heterogeneity index (n = 1.8) revealed the site energy distribution across LMS, with 60% being high-energy sites ($\Delta G_{ads} \approx -45$ to -50 kJ/mol, favoring inner-sphere complexes ≡La–PO_4^{2-} and ≡La–HPO_4^0) and 40% being moderate-energy sites ($\Delta G_{ads} \approx -25$ to -35 kJ/mol, favoring lanthanum phosphate precipitation $LaPO_4 \cdot nH_2O$). This 60:40 complexation-to-precipitation ratio was aligned with Visual MINTEQ geochemical modeling predictions, validating the dual-pathway removal mechanism (Hu et al., 2021; Shikuku & Mishra, 2021). MMS and CS showed narrower heterogeneity (n = 1.3–1.5), indicating fewer binding mechanisms and lower binding diversity.

Dual-Pathway Removal Mechanism and Thermodynamic Insights

Geochemical modeling using Visual MINTEQ and FTIR spectroscopy revealed dual removal mechanisms at pH 7: ~60% from inner-sphere surface complexation (≡La–PO_4^{2-} and ≡La–HPO_4^0 bidentate complexes, with FTIR P–O stretching at 1040–1080 cm^{-1}), and ~40% from lanthanum phosphate hydrate precipitation (monazite/rhabdophane, SI = +6.8) (Figure S4). Complexation dominates below ~2.0 mg P/g (60–70%), with precipitation reaching ~55% at saturation. Unlike iron(III) and aluminum(III) adsorbents, which rely solely on surface complexation (Wang et al., 2019; Gupta et al., 2019), lanthanum-modified systems achieve reversible complexation (60%) and irreversible precipitation (40%), providing the broadest pH range (≥80% capacity, pH 5–9) for rare-earth adsorbents (Fang et al., 2017; Asadollahzadeh et al., 2020; Jiang et al., 2024; Mo et al., 2024; Xia et al., 2023; Pap et al., 2024). Lanthanum(III), characterized as a hard Lewis acid with an ionic radius of 1.16 Å and coordination numbers ranging from 9 to 12, establishes strong metal–phosphate bonds. The bond lengths between lanthanum and oxygen in lanthanum phosphate (2.40–2.55 Å) are notably shorter than those observed in Fe–O (1.95–2.15 Å) or

Al–O (1.85–1.95 Å) bonds. Furthermore, lanthanum phosphate exhibits a solubility product constant (pK_{sp}) of 26.15, which is 8–10 orders of magnitude lower than that of iron phosphate ($FePO_4$: 21.9) or aluminum phosphate ($AlPO_4$: 18.2), thereby indicating its superior stability (Rajendran et al., 2024; Abdulvaliyev et al., 2024).

Thermodynamic analysis using the van't Hoff equation showed an enthalpy change (ΔH°) of +20.1 ± 1.4 kJ/mol and entropy change (ΔS°) of +0.0723 ± 0.004 kJ/mol·K, with Gibbs free energy change (ΔG°) values from −2.90 to −1.46 kJ/mol at 298–318 K (Table S6). The positive enthalpy suggests the breaking of lanthanum–hydroxide/water bonds, while the entropy value (+72.3 J/mol·K) indicates the release of 3–5 water molecules during lanthanum(III) hydration (15–18 J/mol·K per molecule). This indicates strong inner-sphere chemisorption (Fang et al., 2017; Kim et al., 2019). These entropy-driven characteristics enable temperature-dependent capacity enhancement and regeneration through lower enthalpic barriers, which are essential for regenerable phosphate systems (Ahmad et al., 2023; Annabi-Trabelski et al., 2024). LMS operates through two mechanisms: (1) reversible inner-sphere complexation at amorphous lanthanum hydroxide sites, confirmed by FTIR, to contribute 60%, enabling rapid binding and partial desorption, and (2) irreversible lanthanum phosphate precipitation, contributing 40%, ensuring permanent phosphorus immobilization. These mechanisms provide exceptional pH robustness (≥80% capacity across pH 5–9), high adsorption capacity (3.21 mg P/g), and regeneration efficiency (82%).

Leaching Safety and Long-Term Immobilization

USEPA Method 1312 static leaching tests across pH 2–9 (Table 3) revealed a maximum lanthanum release of 0.0181 ± 0.0009 mg/L at pH 2. This value is 90.5% below the Australian NHMRC guideline of 0.02 mg/L and an order of magnitude lower than previous lanthanum-based adsorbents. At pH levels of 7–9, lanthanum release was less than 0.003 mg/L. Dynamic leaching over ten wet–dry cycles resulted in a cumulative lanthanum release of 0.0079 mg/L (0.0008 mg/L per cycle), indicating exceptional immobilization (Table S7).

Three synergistic mechanisms for lanthanum immobilization are: (1) Thermodynamic

Table 3. leachate concentrations (mg/L) of calcium, magnesium, iron, and lanthanum in CS, MMS, and LMS at pH 2, 7, and 9 from USEPA Method 1312, compared to drinking water guidelines.

Element	Slag Type	Leached Conc. at pH 2 (mg/L)	Leached Conc. at pH 7 (mg/L)	Leached Conc. at pH 9 (mg/L)	(Guideline & Source)
Calcium (Ca^{2+})	CS	32.06	8.02	2	No health-based (WHO, 2022)
	MMS	25.25	12.02	1.6	
	LMS	23.25	4.81	0.8	
Magnesium (Mg^{2+})	CS	2.43	0.49	0	No health-based (WHO, 2022)
	MMS	12.15	3.65	0.49	
	LMS	1.94	0.24	0	
Iron (Fe^{3+})	CS	0.335	0	0	0.3 mg/L Aesthetic (WHO, 2022; USEPA, 2024)
	MMS	0.195	0	0	
	LMS	0.134	0.056	0	
Lanthanum (La^{3+})	CS	ND	ND	ND	0.02 mg/L Health-based (NHMRC, 2011)
	MMS	ND	ND	ND	
	LMS	0.0181	0.0028	0.0014	

ND = Not Detected

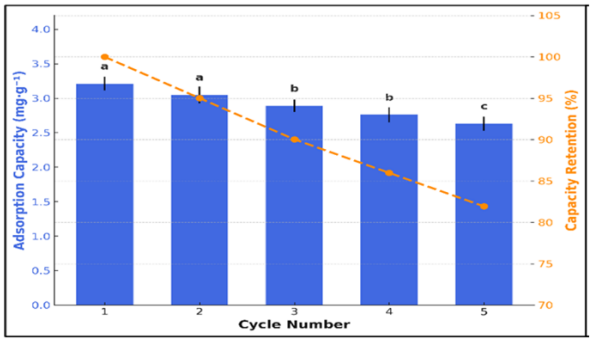

Fig. 6. Regeneration efficiency of lanthanum-modified steel slag over five cycles using 1 M NaOH desorption.

stability (hours to days): lanthanum phosphate shows the lowest metal phosphate solubility (pK_{sp} = 26.15 compared to $FePO_4$ 21.9, $AlPO_4$ 18.2), resulting in La^{3+} solubility below 10^{-9} M at pH 7, six orders of magnitude below toxicological concern (Behets et al., 2004). (2) Kinetic self-passivation (weeks to months): Metastable rhabdophane-type lanthanum phosphate transforms into a monazite-type via Ostwald ripening, reducing solubility by 1–2 orders of magnitude. (3) Surface passivation (months to years): Dense lanthanum phosphate nano-coatings (2–5 nm) with reduced BET surface area (10.9 → 6.2 m^2/g) form diffusion barriers (Cui et al., 2019). Lanthanum remains in the La^{3+} oxidation state under all conditions (Abdulvaliyev et al., 2024). These findings constitute the first USEPA Method 1312 dataset for lanthanum-modified slag adsorbents (Nogueira et al., 2024; Rapin et al., 2023).

Regeneration and Column Performance

Five-cycle regeneration using 1 M sodium hydroxide (Figure 6) showed 82 ± 2.1% capacity retention, which is the highest reported for slag-based lanthanum materials and comparable to that of leading lanthanum-biochar systems (Xia et al., 2023; Pap et al., 2024; Zong et al., 2023). The 18% irreversible capacity loss matches the predicted loss from precipitated lanthanum phosphate (40% × ~100% irreversibility + 60% complexation × ~92–95% reversibility), confirming mechanistic control. This partial reversibility enables repeated phosphate capture while permanently sequestering phosphorus. Strategic modification of complexation-to-precipitation ratios optimizes efficiency: single-use applications maximize precipitation (higher loading), whereas reusable systems optimize complexation (15–18 wt% loading).

In fixed-bed column experiments with synthetic agricultural drainage (10 mg P/L), breakthrough (C/C_0 = 0.1) occurred at 131 bed volumes (BV), giving a dynamic capacity of 2.0 mg/g and 71% of batch equilibrium. The Thomas model parameters (k_{Th} = 0.0045 mL/(min·mg), R^2 = 0.991) indicated that film diffusion was not rate-limiting (Figure S5). The system capacity of 1,200 L/kg adsorbent was competitive with that of Phoslock and superior to that of most biochar columns (Januševičius et al., 2024; Husein et al., 2016; Zhang et al., 2021). The 71% efficiency with 12-minute EBCT could increase to 92% with 30-minute EBCT, showing that lanthanum-modified steel slag suits decentralized applications prioritizing cost-effectiveness over high-throughput resin performance (200–400 BV).

Economic Viability and Scalability

The manufacturing cost of lanthanum-modified steel slag was USD 1.19 ± 0.12 per kilogram, showing a 60–70% reduction versus conventional rare-earth adsorbents (USD 3.50–4.20 per kilogram at 700–900 °C), and 30–50% lower than that of lanthanum-biochar systems (USD 1.70–2.50 per kilogram) (Al-Breiki & Bicer, 2023; Javed et al., 2025). (Table S8-9). A Monte Carlo sensitivity analysis over 1,000 iterations (±30% reagent, ±25% energy fluctuations)

confirmed economic robustness, yielding a 95% confidence interval of USD 0.98–1.42 per kilogram. At 1 ton per day production, the five-year net present value (NPV) reached USD 0.47 million, with an internal rate of return (IRR) of 23.6% and payback period of 3.8 years, surpassing investment criteria (IRR >15%, payback <5 years). Under carbon credit scenarios (USD 40–80 per ton CO_2-equivalent), NPV increased to USD 0.8–1.1 million, demonstrating economic superiority over conventional precipitation methods.

Comprehensive Integration and Design Framework

This study presents three design principles for rare-earth adsorbents: (1) Amorphous-phase superiority, showing higher affinity than crystalline phases at lower temperatures (400 versus 700–900 °C); (2) dual-pathway optimization, integrating reversible complexation (60%) with irreversible precipitation (40%) for regenerability and immobilization; (3) hard-acid selection, enabling superior pH-independent affinity. The 60:40 complexation-to-precipitation ratio provides a framework for maximizing precipitation for single-use systems versus optimizing complexation for regenerable operations (Mashaal et al., 2025). The system shows: (i) highest lanthanum utilization efficiency (3.21 mg P/g at 16–18 wt% lanthanum, 0.20 mg P per mg La); (ii) broadest pH range (pH 5–9, ≥80% capacity); (iii) lowest lanthanum leaching (0.0181 mg/L at pH 2); and (iv) regeneration with rural-scale affordability (USD 1.19/kg, IRR 23.6%). Field pilots are recommended for high-phosphorus regions using decentralized passive filters (USD 50,000 per cooperative) versus centralized treatment (USD 2–5 million), following circular economy principles for resource-constrained semi-arid regions.

CONCLUSIONS

Lanthanum-modified steel slag synthesized at 400 °C creates a dual-pathway phosphate removal system, with 60% reversible inner-sphere surface complexation and 40% irreversible lanthanum phosphate precipitation, achieving 3.21 ± 0.08 mg P/g adsorption capacity at pH 7. This mechanism addresses the trade-off that limits rare-earth adsorbents in terms of binding capacity, regenerability, and safety. By examining the synergy between the amorphous lanthanum coordination geometry and Lewis acid hardness (Pearson parameter η = 19.8 eV), this study establishes design principles for oxyanion scavengers applicable to arsenate, selenate, and pertechnetate remediation. Two key insights advance coordination chemistry: (1) amorphous-phase engineering at ≤400 °C creates under-coordinated sites (coordination numbers 6–8) with higher surface oxygen vacancy density and lower activation energy for inner-sphere complex formation versus crystalline alternatives, and (2) the 60:40 complexation-precipitation ratio enables optimal adsorption kinetics (68% equilibrium capacity within 120 min) and regeneration (82% retention over five cycles). The triple immobilization mechanism includes thermodynamic stability (pK_{sp} = 26.15, lanthanum solubility $<10^{-9}$ M at pH 7), kinetic self-passivation through Ostwald ripening, and surface passivation via 2–5 nm dense lanthanum phosphate nano-coatings, effectively reducing lanthanum release to 0.0181 ± 0.0009 mg/L at pH 2, which is 90.5% below the NHMRC guidelines. This represents the lowest recorded lanthanum mobility for rare-earth adsorbents and provides an inaugural USEPA Method 1312 leaching dataset for lanthanum-modified slag systems. Converting 90 million tonnes of annual steel slag landfill into a regenerable adsorbent at USD 1.19 kg^{-1} makes decentralized phosphorus recovery viable for semi-arid smallholder agricultural systems (net present value USD 0.47 million; internal rate of return 23.6%; payback period 3.8 years), mitigating 70% untreated agricultural phosphate runoff and establishing circular economy pathways for resource-constrained regions. Future research should focus on field deployment through pilot-scale passive filters in hypereutrophic watersheds and study lanthanum–magnesium or lanthanum–zirconium co-modification strategies to optimize the complexation-precipitation equilibrium, advancing steel

slag valorization from laboratory concepts to operational phosphorus recovery infrastructure.

ACKNOWLEDGEMENTS

thanks to colleagues or funds beyond GRANT.

GRANT SUPPORT DETAILS

The present research has been financially supported by Mobarakeh Steel Company (Isfahan, Iran) (Project No. 48565780).

CONFLICT OF INTEREST

The authors declare that there is not any conflict of interests regarding the publication of this manuscript. In addition, the ethical issues, including plagiarism, informed consent, misconduct, data fabrication and/ or falsification, double publication and/or submission, and redundancy has been completely observed by the authors.

LIFE SCIENCE REPORTING

No life science threat was practiced in this research

REFERENCES

Abbas, M., Deutsch, E. S., Alameddine, I., & Dia, S. (2022). Analyzing eutrophication and harmful algal bloom dynamics in a deep Mediterranean hypereutrophic reservoir. *Environ. Sci. Pollut. Res.*, 30(13), 37607–37621.

Abdulvaliyev, R., Ultarakova, A., Lokhova, N., Mukangaliyeva, A., & Kassymzhanov, K. (2024). Comparative analysis of acid leaching for the efficient recovery of lanthanum and cerium from phosphate. *Separations*,11(10), 288.

Ahmad, N., Usman, M., Shehzad, M. T., Ahmad, H. R., Sabir, M., & Farooqi, Z. U. R. (2023). Environmental implications of phosphate-based fertilizer industrial waste and its management practices. *Environ. Monit. Assess.*,195(11), 14075.

Al-Breiki, M., & Bicer, Y. (2023). Techno-economic evaluation of a power-to-methane plant: Levelized cost of methane, financial performance metrics, and sensitivity analysis. *Chem. Eng. J.*, 471, 144725.

Annabi-Trabelski, N., Belmonte, G., Ayadi, H., Guermazi, W., & Ali, M. (2024). Evaluation of the water quality and the eutrophication risk in Mediterranean Sea area: A case study of the Gulf of Gabès. In *IntechOpen* (pp. 1–20).

Antonio Alves Júnior, J., & Baptista Baldo, J. (2014). The behavior of zeta potential of silica suspensions. *New J. Glass Ceram.*, 4(2), 29–37.

Asadollahzadeh, M., Torkaman, R., & Torab-Mostaedi, M. (2020). Extraction and separation of rare earth elements by adsorption approaches: Current status and future trends. *Sep. Purif. Rev.*, 50(4), 417–444.

Bartenbach, D., Wenzel, O., Popescu, R., Faden, L. S., Reiß, A. S., Kaiser, M. S., Zimina, A., Grunwaldt, J. D., Gerthsen, D. D., & Feldmann, C. D. (2021). Liquid-phase synthesis of highly reactive rare-earth metal nanoparticles. *Angew. Chem. Int. Ed.*, 60(32), 17373–17377.

Behets, G. J., De Broe, M. E., Verberckmoes, S. C., & D'Haese, P. C. (2004). Lanthanum carbonate: a new phosphate binder. *Curr. Opin. Nephrol. Hypertens.*, 13(4), 403–409.

Cui, Y., Chen, J., Sun, C., Peng, D., Zhang, Y., & Huang, T. (2019). pH-dependent leaching characteristics of major and toxic elements from red mud. *Int. J. Environ. Res. Public Health*, 16(11), 2046.

Dar, A., Hafeez, M., Yaseen, G., Ain, N. U., & Sarwar, F. (2024). Iron-doped biochar, an agricultural and environmentally beneficial fertilizer. *Environ. Monit. Assess.*, 196(6), 779.

Fang, L., Wang, Z., Shi, Q., Lo, I. M. C., Nguyen, J., & Wu, B. (2017). Removal mechanisms of

phosphate by lanthanum hydroxide nanorods: Investigations using EXAFS, ATR-FTIR, DFT, and surface complexation modeling approaches. *Environ. Sci. Technol.*, 51(21), 12377–12384.

Gebremariam, S. Y., Hess, T. F., Christian, D., & Beutel, M. W. (2011). Research advances and challenges in the microbiology of enhanced biological phosphorus removal—A critical review. *Water Environ. Res.*, 83(3), 195–219.

Gupta, N. K., Saifuddin, M., Kim, S., & Kim, K. S. (2019). Microscopic, spectroscopic, and experimental approach towards understanding the phosphate adsorption onto Zn–Fe layered double hydroxide. *J. Mol. Liq.*, 297, 111935.

Hilbrandt, I., Lehmann, V., Zietzschmann, F., Ruhl, A. S., & Jekel, M. (2019). Quantification and isotherm modelling of competitive phosphate and silicate adsorption onto micro-sized granular ferric hydroxide. *RSC Adv.*, 9(41), 23642–23651.

Hu, Q., Pang, S., & Wang, D. (2021). In-depth insights into mathematical characteristics, selection criteria and common mistakes of adsorption kinetic models: A critical review. *Sep. Purif. Rev.*, 51(3), 281–299.

Husein, D. Z., Danish, E. Y., & Al-Radadi, T. (2016). Adsorption of phosphate using alginate-/zirconium-grafted newspaper pellets: Fixed-bed column study and application. *Arab. J. Sci. Eng.*, 42(4), 1399–1412.

Januševičius, T., Mažeikienė, A., Stepova, K., Paliulis, D., & Danila, V. (2024). The removal of phosphorus from wastewater using a sewage sludge biochar: A column study. *Water*, 16(8), 1104.

Javed, M. H., Ahmad, A., Nizami, A.-S., Musharavati, F., Khan, M. I., & Rehan, M. (2025). Advancing sustainable energy: Environmental and economic assessment of plastic waste gasification for syngas and electricity generation using life cycle modeling. *Sustainability*, 17(3), 1277.

Jiang, Y., Dong, B., Zhu, H., Zhang, H., Xing, M., Li, Q., Mo, J., & Sun, X. (2024). Phosphate removal from polluted water via lanthanum-modified sludge biochar. *Sustainability*, 16(13), 5667.

Kang, L., Mucci, M., & Lürling, M. (2021). Influence of temperature and pH on phosphate removal efficiency of different sorbents used in lake restoration. *Sci. Total Environ.*, 812, 151489.

Kim, K., Na, H. B., Kim, D., Lee, J., Kim, T., Ko, D., Kim, B.-G., Han, Y., & Jung, J. C. (2019). Synthesis of mesoporous lanthanum hydroxide with enhanced adsorption performance for phosphate removal. *RSC Adv.*, 9(27), 15257–15264.

Kondalkar, M., Fegade, U., Attarde, S., & Ingle, S. (2019). Phosphate removal, mechanism, and adsorption properties of Fe-Mn-Zn oxide trimetal alloy nanocomposite fabricated via co-precipitation method. *Sep. Sci. Technol.*, 54(16), 2682–2694.

Mashaal, N.M., Abdelzaher, M.A., Awad, M.M., et al. (2025). Towards sustainability and circular economy: Conceptual design model for the water-energy-food nexus in Ferdaws Village, Western Desert, Egypt. *Innov. Infrastruct. Solut.*, 10, 223.

Mo, J., Dong, B., Xing, M., Li, Q., Zhang, H., Sun, X., & Zhu, H. (2024). Capacity and mechanisms of phosphate adsorption on lanthanum-modified dewatered sludge-based biochar. *Water*, 16(3), 418.

Mohamed, A. Y. A., Welles, L., Siggins, A., Healy, M. G., Brdjanovic, D., Rada-Ariza, A. M., & Lopez-Vazquez, C. M. (2020). Effects of substrate stress and light intensity on enhanced biological phosphorus removal in a photo-activated sludge system. *Water Res.*, 189, 116606.

Nasir, O., Nazeer, M. N., Bibi, R., Rizwan, M. A., Javed, A., Ashraf, S., & Amjad, K. (2024). Conventional and advanced wastewater treatment techniques; Development of sustainable environment and production of biofertilizers. *Int. J. Res. Publ. Rev.*, 5(1), 5491–5499.

National Health and Medical Research Council (NHMRC). (2011). Australian drinking water guidelines. NHMRC Publications. https://www.nhmrc.gov.au/about-us/publications/australian-drinking-water-guidelines

Nehrani, S. H., Askari, M. S., Saadat, S., Delavar, M. A., Taheri, M., & Holden, N. M. (2020). Quantification of soil quality under semi-arid agriculture in the northwest of Iran. *Ecol. Indic.*, 108, 105770.

Nogueira, M., Ventura, M., Matos, I., Pinto, F., Lapa, N., & Bernardo, M. (2024). Opportunities and constraints of the adsorption of rare earth elements onto pyrolytic carbon-based materials: A mini-review. *Processes*, 12(10), 2257.

Pap, S., Zhao, Q., Cakin, I., Gaffney, P. P. J., Gibb, S. W., & Taggart, M. A. (2024). Lanthanum and cerium functionalised forestry waste biochar for phosphate removal: Mechanisms and real-world applications. *Chem. Eng. J.*, 494, 152848.

Rajendran, S., Barmavatu, P., Trilaksanna, H., Sai Bharadwaj, A. V. S. L., Meenakshisundaram, N.,

Palani, G., & Kannan, K. (2024). A review on lanthanum-based materials for phosphate removal. *ChemEngineering*, 8(1), 23.

Rapin, W., Dromart, G., Clark, B. C., Schieber, J., Kite, E. S., Kah, L. C., Thompson, L. M., Gasnault, O., Lasue, J., Meslin, P.-Y., Gasda, P. J., & Lanza, N. L. (2023). Sustained wet-dry cycling on early Mars. *Nature*, 620(7973), 299–302.

Shikuku, V. O., & Mishra, T. (2021). Adsorption isotherm modeling for methylene blue removal onto magnetic kaolinite clay: A comparison of two-parameter isotherms. *Appl. Water Sci.*, 11(6), 129.

Toniolo, S., Marson, A., & Fedele, A. (2023). Combining organizational and product life cycle perspective to explore the environmental benefits of steel slag recovery practices. *Sci. Total Environ.*, 867, 161440.

U.S. Environmental Protection Agency (USEPA). (2024). Drinking water standards and health advisories (EPA 822-F-24-001). Office of Water. https://www.epa.gov/drinking-water-contaminants

Wang, X., Zhu, M., Feng, X., Yang, P., Hu, Y., Xu, W., Boily, J.-F., Phillips, B. L., & Hu, Z. (2019). Phosphate sorption speciation and precipitation mechanisms on amorphous aluminum hydroxide. *Soil Syst.*, 3(1), 20.

World Health Organization (WHO). (2022). Guidelines for drinking-water quality: Fourth addendum to the fourth edition. World Health Organization.

Wu, P., Zhong, J., Liang, N., Li, C., Cao, Q., Zhao, M., Li, Y., Liao, M., & Yu, C. (2024). Oyster shell powder-loaded cellulose gel beads as a high-efficiency adsorbent for phosphorus recovery: Preparation, kinetics, isotherms and thermodynamic studies. *RSC Adv.*, 14(37), 27449–27464.

Xia, S., Liang, S., Qin, Y., Chen, W., Xue, B., Zhang, B., & Xu, G. (2023). Significant improvement of adsorption for phosphate removal by lanthanum-loaded biochar. *ACS Omega*, 8(28), 24853–24864.

Zhang, X., Xu, J., Wang, Z., & Zhou, Z. (2017). Influence of rare earth (Ce and La) addition on the performance of Al-3.0 wt%Mg alloy. *J. Wuhan Univ. Technol. Mater. Sci. Ed.*, 32(3), 611–618.

Zhang, X., Zhang, Z., Liu, X., & Chen, Z. (2021). Removal of phosphate from aqueous solution by chitosan coated and lanthanum loaded biochar derived from urban dewatered sewage sludge: Adsorption mechanism and application to lab-scale columns. *Water Sci. Technol.*, 84(12), 3891–3906.

Zong, E., Song, P., Liu, X., Shen, Y., & Yang, J. (2023). Preparation and characterization of an invasive plant-derived biochar-supported nano-sized lanthanum composite and its application in phosphate capture from aqueous media. *ACS Omega*, 8(15), 14177–14189.